Earth and Space Science

Key Points:
- Global validation of two weather models of every 1 h within 3 years with Global Positioning System and Moderate Resolution Imaging Spectrometer
- Their performances vary spatial-temporally and the High RESolution model outperforms the reanalysis model (ERA5) in most cases
- The comparison agreements are dependent on both the elevation and the magnitude of water vapor

Correspondence to:
Z. Li,
zhenhong.li@chd.edu.cn

Global Comparisons of ERA5 and the Operational HRES Tropospheric Delay and Water Vapor Products With GPS and MODIS

Chen Yu[1] , **Zhenhong Li[2,3,1]** , and **Geoffrey Blewitt[4]**

[1]COMET, School of Engineering, Newcastle University, Newcastle upon Tyne, UK, [2]College of Geological Engineering and Geomatics, Chang'an University, Xi'an, China, [3]Key Laboratory of Western China's Mineral Resource and Geological Engineering, Ministry of Education, Xi'an, China, [4]Nevada Geodetic Laboratory, Nevada Bureau of Mines and Geology, University of Nevada, Reno, NV, USA

Abstract Precipitable water vapor (PWV) from numerical weather models, such as the latest generation of European Centre for Medium-Range Weather Forecasts (ECMWF) reanalysis (ERA5) and the ECMWF High RESolution (HRES) models, are important to meteorological studies and to error mitigation of geodetic observations such as Interferometric Synthetic Aperture Radar. In this study, we provide global validations of these new weather models with respect to Global Positioning System (GPS, ~13,000 stations) and Moderate Resolution Imaging Spectrometer (MODIS, ~1 km resolution) using data from January 2016 to December 2018 of every 1 h. The global standard deviations of the Zenith Tropospheric Delay (ZTD) differences (DSTDs) between weather models and GPS are 1.69 cm for ERA5 and 1.54 cm for HRES. The global PWV DSTDs between weather models and MODIS are 0.34 cm for ERA5 and 0.32 cm for HRES. The two weather models generally perform better in western North America, Europe, and Arctic by having low ZTD DSTDs (<1.3 cm) or PWV DSTDs (<0.3 cm). HRES also has a low ZTD DSTD of less than 1.3 cm in Antarctic, Japan, New Zealand, and Africa and outperforms ERA5 in most regions of the world, despite the fact that 83% of the HRES PWV values are temporally interpolated (from 6 to 1-h). However, under extreme weather conditions, ERA5 performs better owing to its high temporal resolution (1 h). Our results can be used as a global reference for evaluating uncertainties when utilizing these weather models.

1. Introduction

Precipitable Water Vapor (PWV) is one of the most important greenhouse gases that absorbs the most solar radiation (e.g., Kiehl & Trenberth, 1997). It plays a key role in the hydrological cycle with fundamental impacts on the Earth's climate. Good knowledge of PWV is crucial for meteorological forecasting for extreme hydro-meteorological events (e.g., Millán, 2014), fog occurrences (e.g., Veljović & Vujović, 2019), global lightning activities (e.g., Price, 2000) and tornado-produced storms (e.g., Georgiev, 2003). The spatial-temporal variability of PWV also leads to the changes in the tropospheric delay, which is known to be a common error source in geodetic observations including Global Positioning System (GPS) (e.g., Iwabuchi et al., 2003), Interferometric Synthetic Aperture Radar (InSAR) (e.g., Yip et al., 2019), Very Long Baseline Interferometry (VLBI) (e.g., Eriksson et al., 2014), and satellite altimetry (e.g., Obligis et al., 2011). Such effects prevent InSAR from measuring small magnitude or long wavelength geophysical deformation signals, for instance those resulting from inter-seismic strain accumulation and post-seismic strain relaxation which not only provide insight into the mechanics of faulting systems but also the possibility of future seismic hazards (e.g., Daout et al., 2019; Jolivet et al., 2013). As a result, mitigation of the tropospheric effect has becoming increasingly challenging in recent (e.g., Sentinel-1 and Gaofen-3) and future InSAR missions (e.g., GEOSAR and NISAR, which are due to operate in the next 3–10 years) owing to their unprecedented spatial coverage and temporal resolution of the measurement. Such effects can also degrade the GPS positioning accuracy notably in the network Real Time Kinematic mode due to their impacts on the estimation of tropospheric delay corrections used by users in order to achieve instantaneous cm-level positioning accuracy (G. R. Hu et al., 2003). This is necessitated by applications such as rapid earthquake source determination and tsunami early warning (e.g., Mori et al., 2011), volcanic monitoring (e.g., Zahorec et al., 2018), costal

erosion (e.g., Esposito et al., 2018), landslide monitoring (e.g., Barbarella et al., 2018), railway construction (e.g., Stallo et al., 2018), and intelligent transport systems (e.g., Meng et al., 2018).

Currently, measurements of PWV are often obtained from ground to satellite based sensors, including radiosondes, GPS, Moderate Resolution Imaging Spectrometer (MODIS) on board NASA's Terra and Aqua satellites, as well as numerical weather models (Bevis, 1994; Gao & Kaufman, 2003; Jolivet et al., 2011; Yu et al., 2018). From a geodetic point of view, these products differ in their spatial-temporal resolutions, data availability, and uncertainties. The radiosonde is a telemetry instrument carried into the atmosphere usually by a weather balloon, resulting a vertical profile of various atmospheric parameters. It provides global coverage but at discrete stations so that low in spatial-temporal resolutions (daily or twice daily) owing to the high costs associated with launching radiosonde (Durre et al., 2018). MODIS provides global coverage observations in 36 spectral bands, among which five near-infrared bands are used to calculate ~1 km spatial resolution PWV over clear land areas of the globe. Despite its dense spatial resolution, MODIS has only a daily sampling rate and observations are only available under cloud-free conditions and is claimed to be determined with an accuracy of 5%–10% (Gao & Kaufman, 2003). GPS retrieves the pointwise Zenith Tropospheric Delay (ZTD), which can be used to obtain PWV using surface pressure and temperature (Bevis, 1994), at each ground station by combining satellite range and/or phase observations at different incidence angles with minutes to hours temporal resolutions depending on its sampling rate (Ahmed et al., 2016). However, the distribution and the density of GPS stations, usually installed around urban areas, may limit its usage in the determination of continuous 2D ZTD/PWV fields. Previous studies have reported inconsistent and different PWV Root Mean Square (RMS) differences. Comparisons between GPS and MODIS PWV products showed that MODIS PWV appeared to overestimate water vapor compared to GPS values with a scale factor of about 1.05 and MODIS and GPS water vapor products agreed to within 1.6 mm in terms of standard deviations (Li et al., 2005, 2009). Liu et al. (2013) reported a 1.3 mm RMS between radiosonde and MODIS PWV over Hong Kong. Gurbuz and Jin (2017) showed 5.0 mm RMS differences between GPS and MODIS over Turkey. Prasad and Singh (2009) showed a 7.8 mm RMS difference between GPS and MODIS PWV over India but Li et al. (2003) showed a 1.7 mm standard deviation of the differences over Germany. These inconsistences arose as most of these studies were conducted in a local region or on discrete points, but the water vapor quality derived from different techniques may vary both spatially and temporally.

Numerical weather models use mathematical models of the atmosphere combined with current meteorological observations to provide predictions on atmospheric variables which are in turn used to predict the future weather states, such as the Weather Research and Forecasting (WRF) model, the European Centre for Medium-Range Weather Forecasts (ECMWF) and many other global and regional weather models run by local meteorological departments. These models are constantly updated based on new observations or improved mathematical models, for example, on March 8, 2016, ECMWF improved the spatial resolution of its High RESolution (HRES) atmospheric analysis model to ~9 km from ~16 km with a 6-h temporal resolution, and from early 2019, ECMWF started to publish the fifth generation reanalysis model (ERA5) with 1-h temporal and ~25 km spatial resolutions (the entire ERA5 data set from 1950 to present should gradually become available before the end of 2020), which is a replacement of the previous ERA-Interim model (6-h temporal and ~75 km spatial resolutions, expired on August 31, 2019). Given these spatially regular and temporally continuous resolutions, and global availability, the weather model derived PWV has been extensively used not only in meteorology (e.g., Lin et al., 2016) but also in geodesy and geophysics, notably the mitigation of the atmospheric error in geodetic observations such as InSAR (e.g., Jolivet et al., 2014), GPS (e.g., Zhu et al., 2018), and VLBI (e.g., Boehm & Schuh, 2007). However, prior to the utilization of these state-of-art weather models, it is necessary and urgent to evaluate its accuracy in order to understand and quantify the uncertainty that may be introduced to the users' applications, which is therefore addressed in this study.

Previous studies have used GPS to validate ERA-Interim and showed a mean difference of 1.1 cm and a RMS difference of 2.4 cm between GPS and ERA-Interim ZTDs over China (Chen et al., 2011), and less than 0.4 cm differences between ERA-Interim and GPS PWV over North America (Bordi et al., 2016). As for the new weather models, Cliffe Ssenyunzi et al. (2020) reported a 0.17 cm RMS difference between ERA5 and GPS PWV on 13 GPS stations over eastern Africa and Jiang et al. (2020) reported a 0.3 cm mean difference

and a 1.15 cm RMS difference between ERA5 and GPS ZTDs over China. However, there is a lack of studies about validation of the HRES ECMWF product, despite its reported successful usages such as in InSAR atmospheric correction (e.g., Anantrasirichai et al., 2019; Z. Hu & Mallorquí, 2019; Murray et al., 2019; Yu et al., 2018). Furthermore, previous validations of the new ERA5 product have focused mainly on regional scales and on a pointwise basis, and, most importantly, the spatial-temporal variability of its comparison statistics was not investigated, despite the fact the weather models' performances may have a heterogeneous global distribution. As a result, in this study, we seek to validate HRES and ERA5 using ~13, 000 globally distributed GPS stations and the 1-km global MODIS PWV maps. Their agreements, and the spatial-temporal variability of the agreements, are investigated globally every 1 h from January 2016 to December 2018, providing a comprehensive understanding of the weather model PWV uncertainty and a general reference for users utilizing their products.

2. Data and Method

A variety of datasets were used in this study, including the ground-based GPS ZTD estimates, space-based MODIS PWV observations and the ECMWF weather model outputs. Specifically, we aim to compare the two different ECMWF weather models against GPS ZTDs and MODIS PWV on a global scale from January 2016 to December 2018 in order to investigate, if any, systematic and stochastic disagreements among them. GPS provides high accuracy ZTD estimates which is often used to validate weather models (e.g., Chen et al., 2011) and its high temporal resolution plays a key role in evaluating the temporal variability of the weather model product. MODIS provides high spatial resolution PWV observations which is especially valuable in evaluating the spatial variability of water vapor (e.g., Li et al., 2003).

2.1. Whether Models (HRES and ERA5)

HRES is an operational ECMWF climate analysis model which combines short-range forecast data with observations to produce the best fit to both. It provides a large number of atmospheric, land and oceanic climate variables every 6 h with a spatial resolution of ~10 km and in near real-time (with a 5–10 h delay, https://www.ecmwf.int/en/forecasts/datasets/set-i).

ERA5 is a new ECMWF climate reanalysis model which replaces ERA-Interim (stopped being produced on August 31, 2019) and provides a numerical description of the recent climate by combining models with observations. It provides hourly estimates of climate variables at a spatial resolution of ~25 km. Quality-assured monthly updates of ERA5 are published with a 3-month delay. Preliminary daily updates of the data set are available to users with a 5-day delay.

Apart from their differences in spatial-temporal resolutions, with ERA5 having a higher temporal resolution and a lower spatial resolution than HRES, ERA5 utilizes the Integrated Forecasting System (IFS) Cycle 41r2 with several added features specifically developed for reanalysis throughout the data period, whilst HRES-ECMWF uses continually updated IFSes which changed from Cycle 41r1 to Cycle 41r2 since March 2016, to Cycle 43r1 since November 2016, to Cycle 43r3 since July 2017 and to Cycle 45r1 since June 2018 (https://www.ecmwf.int/en/publications/ifs-documentation). Furthermore, the two products use slightly different satellite and in situ observations.

For each 10-km grid for HRES and 25-km grid for ERA5, the surface pressure and 137 vertical levels of temperature and specific humidity variables were used to calculate its ZTD and PWV as described in Jolivet et al. (2011). In this study, global HRES (10-km of every 6 h) and ERA5 (25-km of every 1 h) ZTD and PWV maps from January 1, 2016 to December 31, 2018 were used.

2.2. GPS ZTD Product

We used globally distributed ~13,000 GPS stations (Figure 1). The 5-min ZTD time series at each station was estimated by GipsyX using JPL final GPS orbit and clock solutions at Nevada Geodetic Laboratory, University of Nevada (Blewitt et al., 2016). The ZTD and its horizontal gradients were estimated as random walk with process noises of 5.0d–8 km/sqrt(sec) and 5.0e−9 km/sqrt(sec), respectively. A full description of the GPS data processing strategy can be found at http://geodesy.unr.edu/gps/ngl.acn.txt.
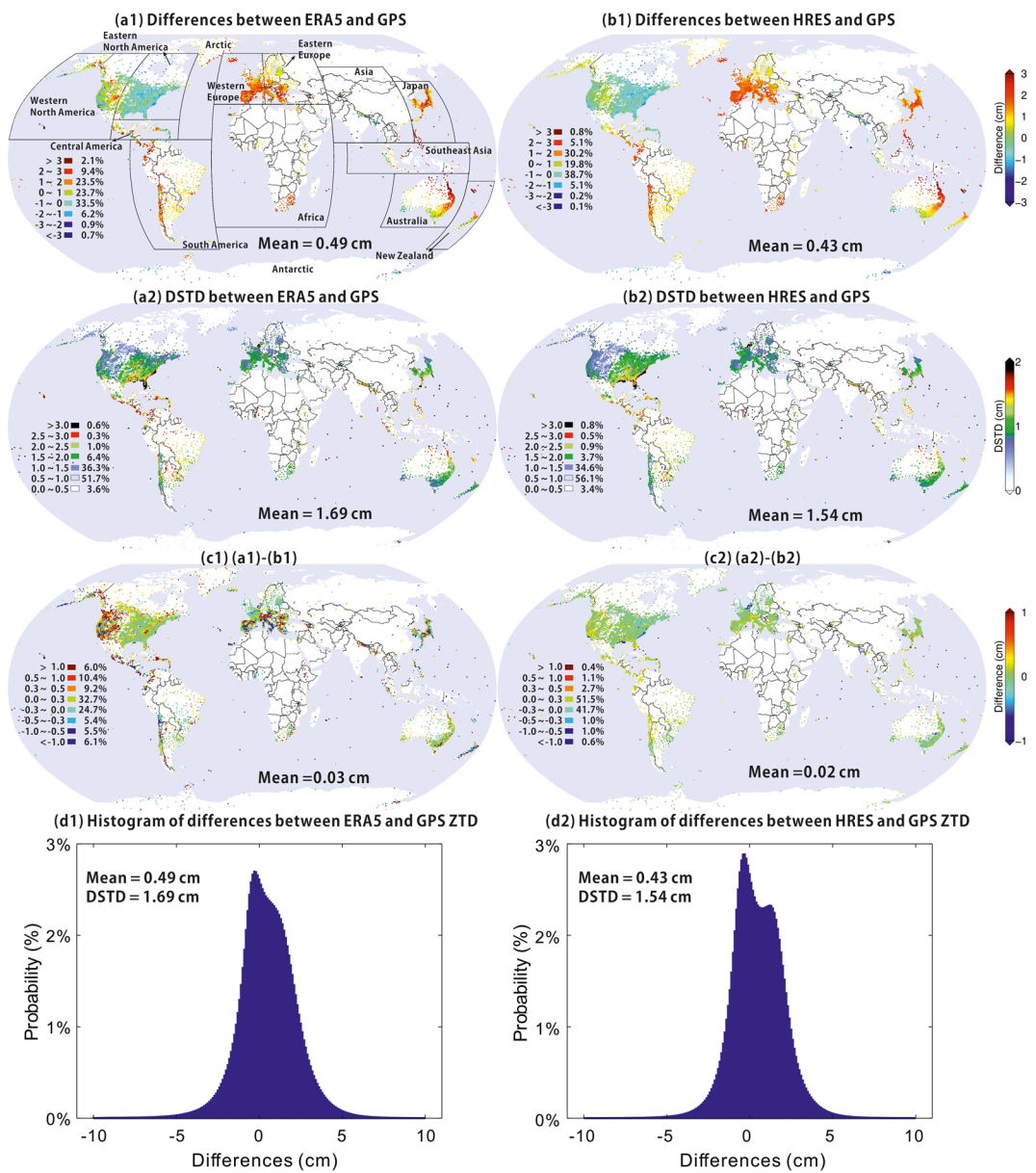
Figure 1. ZTD comparisons between ERA5 and GPS (a) and between HRES and GPS (b) using hourly data from January 2016 to December 2018. (a1 and b1) are the mean difference of each station. (a2 and b2) are the DSTD of each station. (c1) is the difference between (a1) and (b1). (c2) is the difference between (a2 and b2). (d1 and d2) are the histogram of the ZTD differences for ERA5 and HRES in (a1 and b1), respectively. GPS, Global Positioning System; HRES, High RESolution; ZTD, Zenith Tropospheric Delay.

We did not include the GPS PWV product, given the fact that it is retrieved first by separating the wet delay component from the hydrostatic delay component using surface pressure over or near the GPS station (e.g., Elgered et al., 1991), and then by approximating the weighted mean temperature (Tm, the average temperature of atmosphere weighted by the pressure of water vapor) to covert the wet delay to PWV (Bevis et al., 1992). Note that Tm should be dependent not only on surface temperature, but also on the tropospheric temperature profile and the vertical distribution of humidity (Davis et al., 1985), and an empirically derived linear regression might lead to additional uncertainties in the PWV estimate (e.g., Webley et al., 2002). Furthermore, atmospheric corrections for geodetic observations including GNSS, InSAR, VLBI and satellite altimetry as mentioned in the Introduction section require ZTD, rather than PWV, since the hydrostatic delay component also plays an important role (e.g., Jolivet et al., 2014).

2.3. MODIS PWV Product

We used the near-infrared Level-2 MODIS PWV product which are generated at ∼1 km spatial resolution using the near-infrared algorithm during the day. The algorithm estimates the water vapor from the transmittance, based on theoretical radiative transfer calculations and a look-up-table procedure, with an accuracy of 5%–10%, but the errors will be greater for retrievals from data collected over dark surfaces or under hazy conditions (Gao & Kaufman, 2003). In order to minimize (if not avoid) the uncertainty in MODIS PWV due to the presence of clouds, we used the level-2 MODIS cloud product to mask out the cloudy pixels so that only clear pixels with a confidence level of greater than 99% as defined in Frey et al. (2008) were used. The elevation of each MODIS PWV pixel was interpolated from the 30 m Shuttle Radar Topography Mission (SRTM) global Digital Elevation Model (DEM) for the region between latitude −60° to 60° (Farr et al., 2007) and from the 30 m Advanced Spaceborne Thermal Emission and Reflection radiometer (ASTER) global DEM for the regions between latitude 60°–83° and −60° to −83° (Team, 2011).

2.4. Methods and Statistics Used

To compare the two weather models against GPS and MODIS, we spatially interpolated respectively the ERA5 and HRES ZTDs onto each GPS station as well as PWV onto each cloud free MODIS pixel based on the Iterative Tropospheric Decomposition (ITD) interpolator (Yu et al., 2017), with the correspondent ZTD and PWV differences calculated. We also linearly interpolated HRES from 6 to 1-h to comply with the temporal resolution of ERA5 and, most importantly, to assess fully the impact of the spatial-temporal resolutions on the weather models. In this way, all the comparisons in this paper were implemented at every hour between 2016 and 2018.

Throughout this study, we used the differences between products and the Difference STandard Deviation (DSTD) to statistically describe the quality of the weather models relative to GPS and MODIS. We also showed the spatial distribution and time series of the DSTD to investigate the stability and spatial-temporal variability of the agreements between the weather models and GPS/MODIS.

3. ZTD Comparisons Between Weather Models and GPS

Figure 1 shows the 3-year mean differences and DSTDs respectively between ERA5 and GPS and between HRES and GPS of each station from January 2016 to December 2018. Notable overestimating of ZTDs for both of the two weather models can be observed in a range of regions such as in Europe, Japan, Australia, and Africa. Regions with dense GPS stations also denoted spatially variant mean differences, with differences in Northwestern Europe being smaller than southwestern Europe, differences in Northeastern Australia (including New Zealand) being greater than southwestern Australia and differences in western South America being greater than the east. Stations in North America have the smallest differences compared to the other regions, with its western stations being greater than the eastern stations. Overall, the HRES global mean difference (0.43 cm) is smaller than the ERA5 counterpart (0.49 cm) as shown in Figure 1c1, particularly in western North America and central Europe. However, HRES has larger differences than ERA5 in regions such as New Zealand and Italy. Fifty-seven and two tenths percentage stations have an absolute difference of less than 1 cm for ERA5 but 58.5% stations for HRES. The difference between ERA5 and HRES mainly occurred in regions of western North America, Southern Europe, Japan, Nepal, and New Zealand as shown in Figure 1c1.

The DSTD of each station is shown in Figures 1a2 and 1b2 where considerable spatial variability is observed. Although large differences (2–3 cm) are found on various regions such as Europe, Japan, and Australia, their DSTDs are small (1–2 cm), implying the differences between weather models and GPS here are generally stable and behave largely as constants. These constant shifts could be introduced by the estimation of an optimal initial state of the atmosphere for the numerical forecast (Gutman & Benjamin, 2001). However, they are less concerned by applications in which only relative ZTDs are used such as the mitigation of InSAR tropospheric errors. Eastern North America has greater DSTDs than the west, which is also observed in the comparisons with MODIS in Section 4, and the east coast of North America including Florida has the greatest DSTD (>3.0 cm). This may due to their different climate systems, resulting the east coast of North America holding more water vapor (Vonder Haar et al., 2012) and more humid (Gaffen &
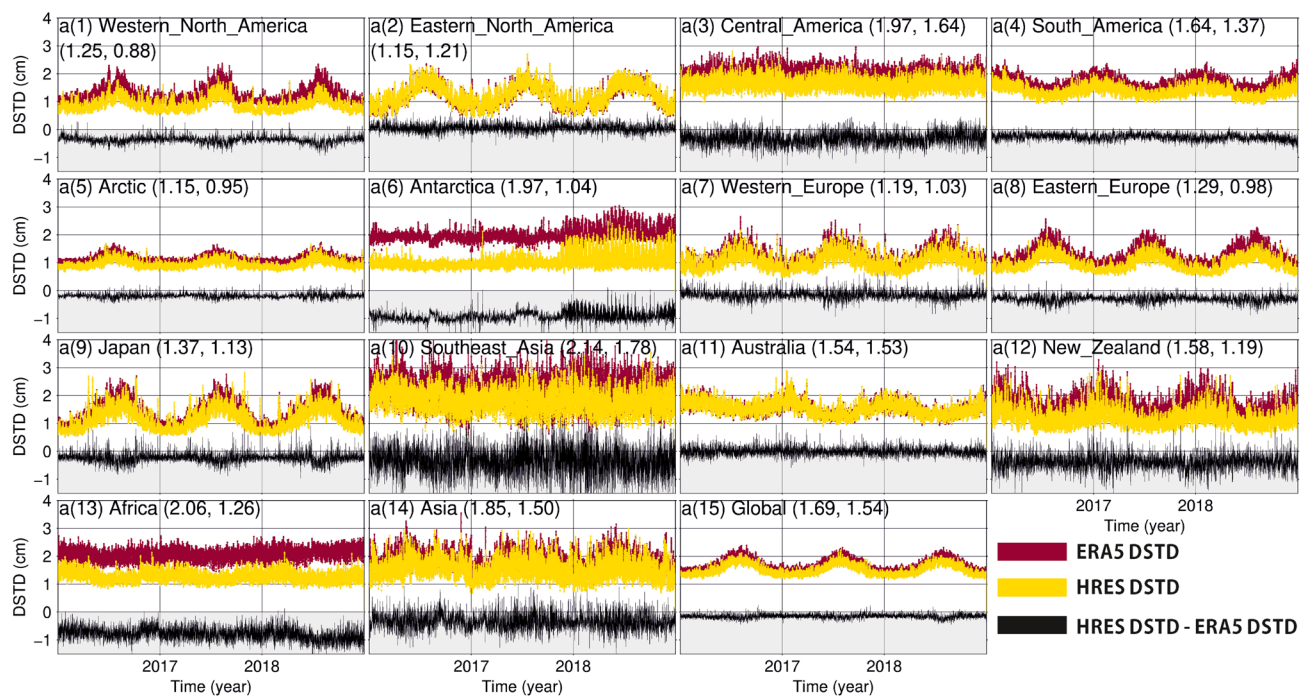
Figure 2. Hourly ZTD DSTD time series respectively between ERA5 and GPS (red) and between HRES and GPS (yellow) per region as defined in Figure 1a1 (a1–a14) and for the globe (a15) from January 2016 to December 2018. The black solid lines denote the correspondent time series of (HRES DSTD–ERA5 DSTD). The numbers in the bracket show the 3 year mean DSTDs sequentially for ERA5 and HRES (unit in cm). GPS, Global Positioning System; HRES, High RESolution; ZTD, Zenith Tropospheric Delay.

Ross, 1999) than the west throughout the year, especially in Florida which was hit by more storms than any other U.S. state. The DSTD shows a certain degree of latitude dependency in regions such as Japan and east of Australia as stations far away from the equator tend to have less water vapor so that smaller DSTDs. This will be discussed further in Section 5.2. The global mean DSTDs respectively for ERA5 and HRES are 1.69 and 1.54 cm. HRES has a lower DSTD than ERA5 on 55.7% of the stations. Only 51.7% stations have a DSTD of less than 1 cm for the ERA5 comparison, compared to 56.1% for the HRES comparison.

In order to validate the weather models temporally, we divided the globe into 14 regions as shown in Figure 1a1 approximately according to their climatic features, the mean ZTD difference distribution, the DSTD distribution and the coverage of GPS stations. For each region, we calculated its DSTD time series between weather models and GPS of all the stations within that region every 1 h as shown in Figure 2. These DSTD time series show considerable seasonal variations which peak in summer (June to August for the Northern hemisphere and December to February for the Southern hemisphere) and drop in winter and coincide with the seasonal variation of water vapor. This implies the weather models agree worse with GPS in summer than that in winter. Since the tropospheric delay has more substantial seasonal variations in temperate latitudes compared to Equatorial (all year high) and Polar (all year low) regions mainly due to the variation of water vapor (Chelton et al., 1981), the DSTD variation in temperate latitudes are generally greater than that in Equatorial and Polar regions, with Japan having the greatest (~1.5 cm peak-to-valley). Apart from the seasonal variation, the fluctuation of the DSTD time series is the greatest in Southeast Asia, owing to the high amount of water vapor, hence large tropospheric delays, of the stations close to the equator. Stations in Arctic, however, have the smallest DSTD fluctuation due to its small water vapor amount and dry atmosphere. Overall, most of the (HRES DSTD–ERA5 DSTD) values are negative, implying that HRES has a better agreement with GPS than ERA5, particularly in Antarctica (1.97 cm for ERA5 compared to 1.04 cm for HRES) and Africa (2.06 cm for ERA5 compared to 1.26 cm for HRES). However, ERA5 performs slightly better than HRES in eastern North America (1.15 cm for ERA5 compared to 1.21 cm for HRES). Their different performances could be caused by the different spatial-temporal resolutions and the forecasting algorithms utilized as described in Section 2.1.
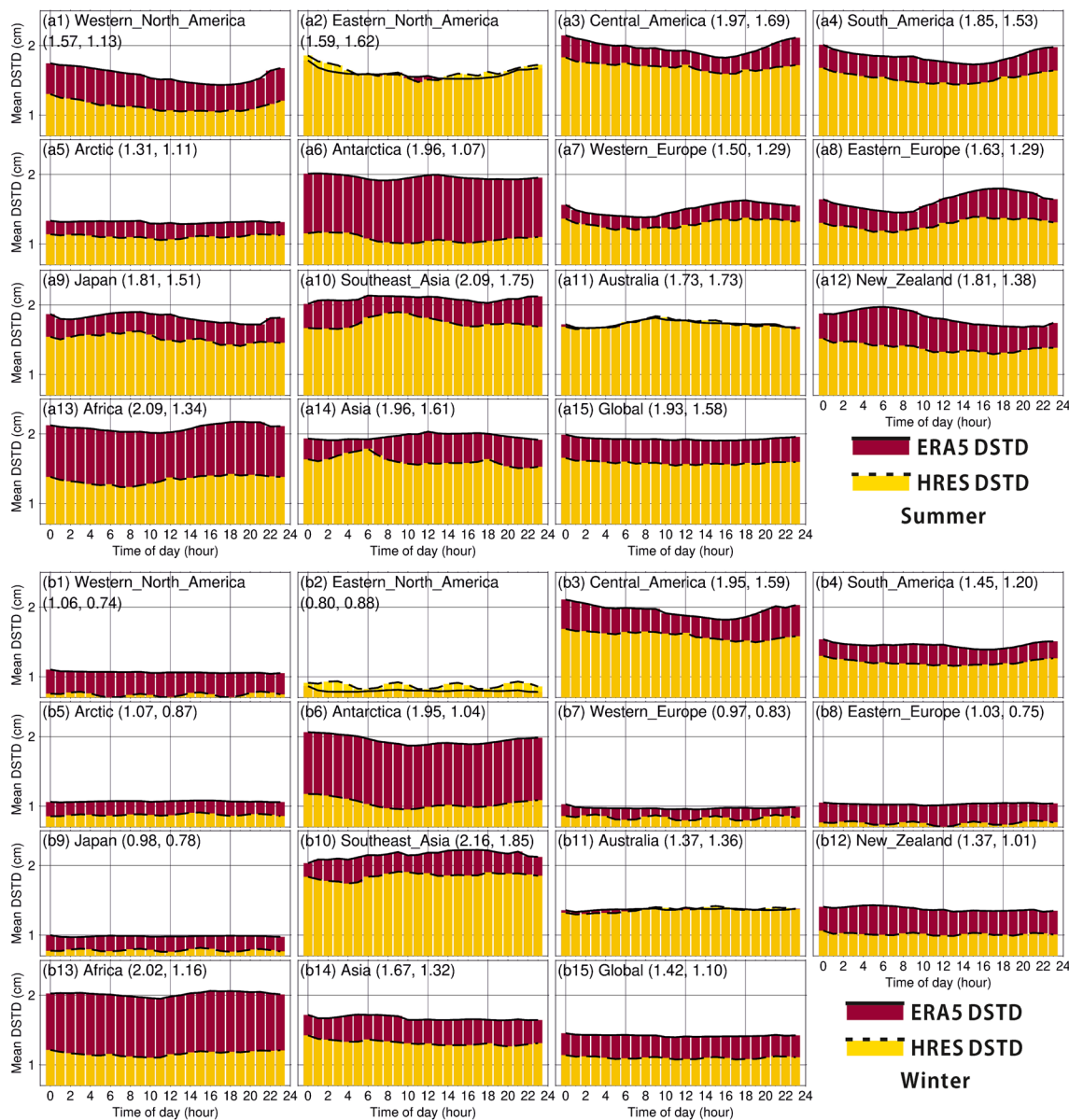
Figure 3. ZTD DSTDs per region between the weather models and GPS for each hour of the day averaged of the summer period (June to August for the North Hemisphere and December to February for the South Hemisphere) and winter period (December to February for the North Hemisphere and June to August for the South Hemisphere), respectively. The numbers in the bracket show the mean DSTDs sequentially for ERA5 and HRES (unit in cm). DSTD, Difference STandard Deviation; GPS, Global Positioning System; HRES, High RESolution; ZTD, Zenith Tropospheric Delay.

Since GPS provides ZTD estimates every 5 min, it is possible to test whether the performance of HRES could retain on each hour throughout the day compared with the hourly sampled ERA5 ZTD, provided that the 1-h HRES ZTD is linearly interpolated from the original 6 h sampling rate. For each hour of the day, we calculated the DSTD per region based on all the stations in that region within 3 years for the summer (Figure 3a) and winter (Figure 3b) periods, respectively. A similar pattern is found as in Figure 2 that HRES outperforms ERA5 in most of the regions by having a lower DSTD, particularly in Antarctica and Africa where the mean ERA5 DSTD is about twice of the HRES DSTD. The DSTD is generally higher and has more diurnal variation in summer than that in winter, as observed in western North America, South America, Europe, Japan, Australia, and New Zealand. On average, the HRES DSTD at 0, 6, 12, and 18 o'clock have not substantially outperformed the other hours, suggesting that the temporally linear interpolation of the HRES ZTD has largely retained its performance. However, in regions such as eastern North America, Western and
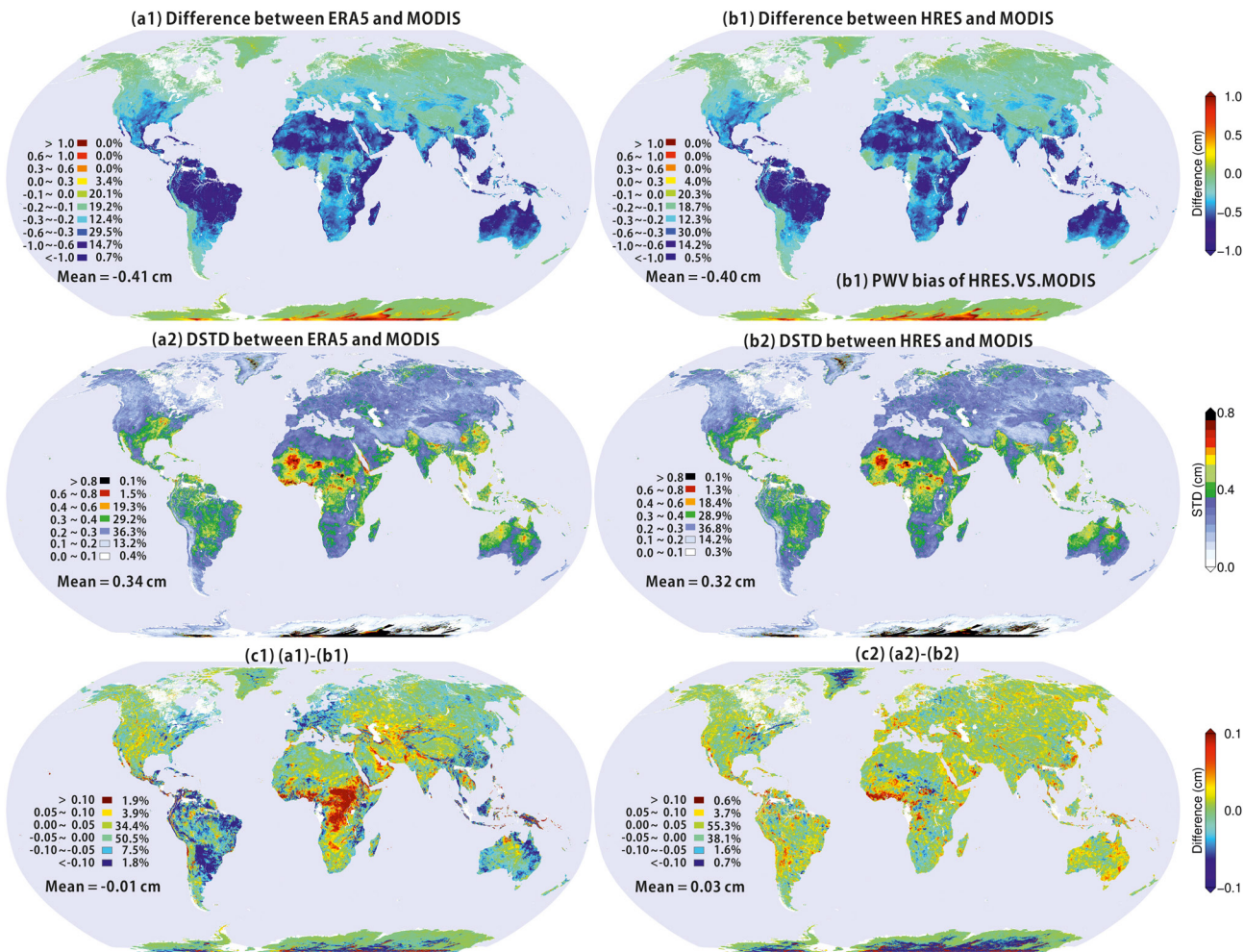
Figure 4. PWV comparisons between the two weather models and MODIS. (a1 and b1) are respectively the mean of (ERA5—MODIS) and (HRES—MODIS) PWV of each 5-km grid from January 2016 to December 2018, with (a2) and (b2) denoting the correspondent DSTD of each grid. (c1) is the difference between (a1 and b1). (c2) is the difference between (a2 and b2). The statistics shown were calculated excluding the pixels over Antarctica. DSTD, Difference STandard Deviation; HRES, High RESolution; ZTD, Zenith Tropospheric Delay.

Eastern Europe, and Japan, there are indeed variations showing HRES having larger DSTDs on 3, 9, 15, and 21 o'clock than the original HRES sampling hours which are not observed on ERA5. This effect is also found to be greater in winter than in summer which is probably due to the fact that the weather models perform better in winter (i.e., low DSTDs), leaving the temporal interpolation error of HRES more dominant. Whereas in summer, other error sources introduced by the high amount of water vapor and its variation may, to some extent, mask the effect caused by the temporal interpolation. The high temporal resolution of ERA5 is superior in maintaining a constant performance throughout the day and crucial in events of rapid changing atmosphere, which will be discussed further in Section 5.3.

4. PWV Comparisons Between Weather Models and MODIS

In this section, we spatially interpolated the hourly ERA5 and HRES PWV onto all the cloud free MODIS pixels at each hour of the day from January 2016 to December 2018. To calculate and display the results considering the irregular distribution of the MODIS pixel, we defined a uniform 0.05° grid (~5 km), containing ~5 original MODIS pixels. For each grid, we calculated the mean PWV difference and DSTD of all the pixels located in that grid within 3 years and plotted in Figure 4. Note that due to the ice cover over Antarctic deteriorating the quality of MODIS PWV (Gao & Kaufman, 2003), this region was excluded in this section.

Overall, MODIS tended to overestimate PWV compared to the weather models, with their mean differences being −0.33 and −0.32 cm for ERA5 and HRES, respectively. The overestimation is also found in previous researches when comparing MODIS to GPS (e.g., Prasad & Singh, 2009; Vaquero-Martínez et al., 2017). Fifty five and one tenth percentage of the grids of ERA5 differ from MODIS by less than 0.3 cm, compared to 55.3% of the grids of HRES. The DSTD maps show that the weather models agree worse with MODIS in southeast of North America (also observed in Figure 1 when comparing with GPS), central Africa, southeast of Asia and northwest of Australia than the other regions. The global mean DSTDs are 0.34 and 0.32 cm for ERA5 and HRES, respectively. On average, HRES outperforms ERA5 despite of its lower temporal resolution and 75% (18 h out of 24) temporally interpolated values. 49.9% of the grids of ERA5 have a DSTD of less than 0.3 cm, compared to 51.3% of HRES. HRES differs from ERA5 the most in central Africa and South America, with ERA5 having relatively larger (absolute values) PWV differences against MODIS in South America and smaller PWV differences against MODIS in central Africa. The HRES DSTD differs from ERA5 the most in the coast of the Gulf of Guinea, Africa, with the ERA5 DSTD being larger than HRES by more than 0.1 cm. The higher resolution of HRES than ERA5 is beneficial in the Gulf of Guinea due to its extreme weather conditions and rainfalls, which plays a key role in the inter-annual variability of the West African monsoon (Joly & Voldoire, 2010).

Noticing the spatial variability of the PWV DSTD in Figure 4, it is necessary to evaluate them individually in different regions and also temporally through the DSTD time series, as have done in Section 3. We used the same regions defined in Figure 1a1 and plotted the daily (as MODIS PWV is sampled daily) PWV DSTD time series in Figure 5. Since MODIS PWV is acquired approximately at the same time per day in each region (e.g., ~10:30 local time around the equator), we also showed in Figure 5c the MODIS acquisition time for each 5-km grid computed by averaging the acquisition time within 3 years. Note that although we plotted here the DSTD time series of Antarctica, the global DSTD time series were calculated excluding this region due to its problematic quality of MODIS PWV. Similar seasonal variations compared to Figure 2 are observed and the variation amplitude reaches 4–5 mm in North America, Arctic and Asia. The two weather models generally perform better (DSTD < 0.3 cm) in western and eastern North America, Arctic, Europe, Japan, New Zealand, and Asia. HRES has smaller DSTDs than ERA5 in 79% of the 14 regions but performs similarly with ERA5 in eastern North America. Central America and Southeast Asia have relatively the largest performance differences (0.03 cm) between ERA5 and HRES. The HRES DSTD is more stable than that of ERA5, with the later having frequently large DSTD jumps, as observed in Western Europe, Japan and Southeast Asia (Figure 5). Although HRES PWV is temporally interpolated from 6 to 1-h, there is no substantial performance degradation at the interpolated hours. For example, observations in Australia, Asia, Western Europe, South America, and Western North America were mostly acquired at non HRES sampling hours but the HRES DSTDs in these regions are smaller or similar compared with ERA5. However, under extreme weather conditions, one may also benefit from the high temporal resolution of ERA5 which will be further discussed in Section 5.3.

5. Discussion

We have shown that the performances of the two weather models validated by GPS and MODIS vary from place to place and over time. In this section, we will statistically investigate their performance dependencies on the elevation and the magnitude of ZTD/PWV.

5.1. Elevation Dependency

Considering the elevation dependency is important in a way that water vapor is strongly correlated with the elevation and highly variable around mountainous terrain due to complex patterns of air flow associated with high reliefs (Webb et al., 2020). We plotted in Figure 6 the DSTD per station against the elevation for each region defined in Figure 1a1 using the 3 year data. It is clear that DSTDs are generally inversely correlated with the elevation as expected, since high-altitude stations tend to have smaller ZTDs than low-altitude stations. Nearly all large DSTD jumps (>2 cm) occur at low altitudes (<500 m). High-altitude stations also contribute to a narrower scattered DSTD distribution than low-altitude stations, indicating good and stable agreements with GPS. However, in areas such as eastern North America, eastern Europe, and Japan, some of the low-altitude stations have better agreements with GPS than the high-altitude stations. The
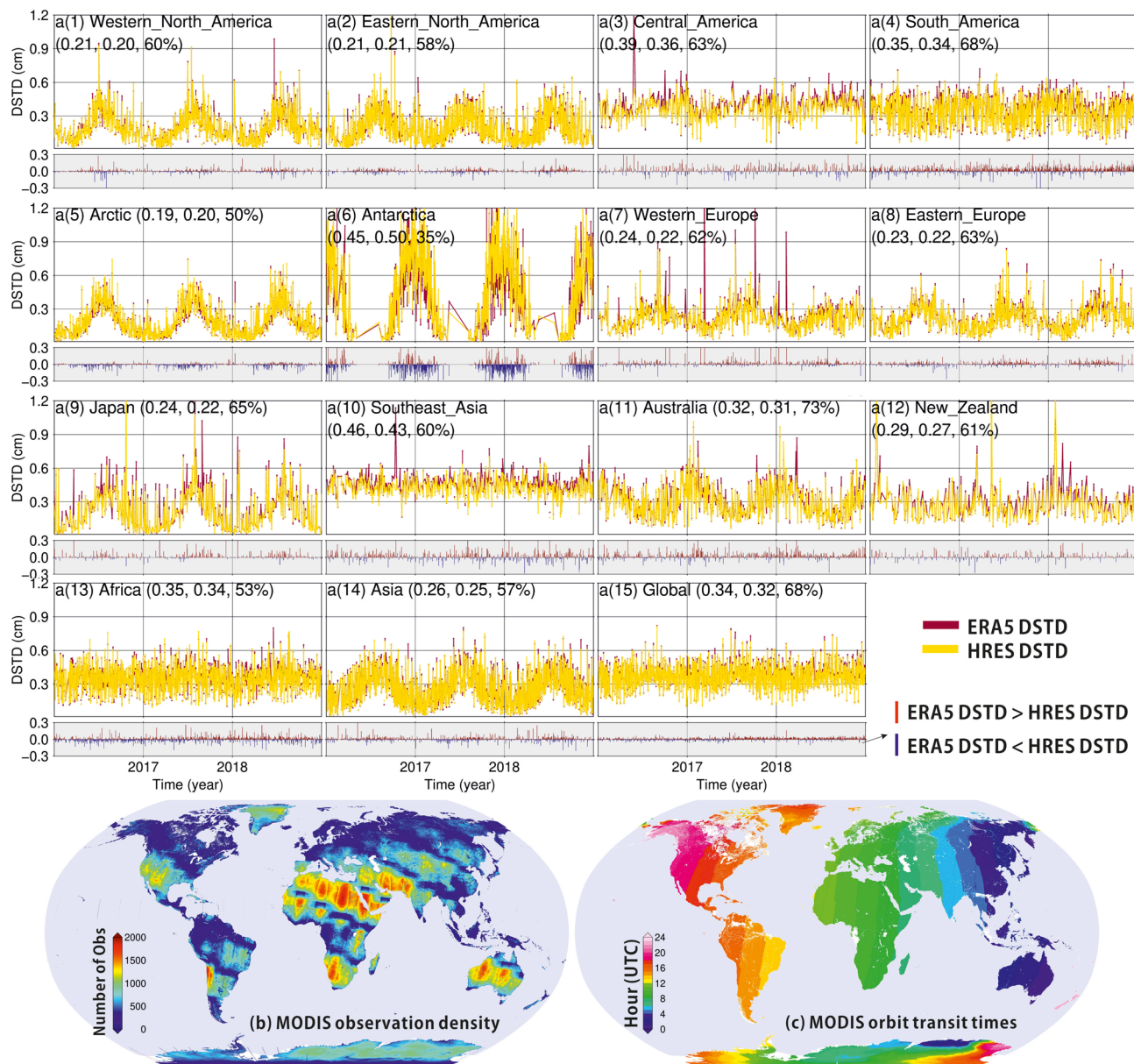
Figure 5. Daily PWV DSTD time series between weather models and MODIS from January 2016 to December 2018 for each region defined in Figure 1a1. The bottom colored bars indicate the difference between ERA5 and HRES DSTDs (red: HRES < ERA5; blue: HRES > ERA5). The numbers in the bracket of each caption show respectively the mean ERA5 DSTD, the mean HRES DSTD, and the percentage of dates when the ERA5 DSTD is larger than the HRES DSTD. (b) shows the number of observations in each grid for 3 years. (c) shows the data acquisition time (hours in UTC) of each grid averaged from 3 years of data. DSTD, Difference STandard Deviation; HRES, High RESolution; MODIS, Moderate Resolution Imaging Spectrometer; PWV, precipitable water vapor.

correlation slope between the DSTD and elevation ranges from −0.01 to −0.55, corresponding to a decrease of the DSTD of 0.01–0.55 cm per 1 km. The global mean correlation coefficients are 0.18 for ERA5 and 0.28 for HRES, respectively, and the largest correlation coefficient occurs in Central America for ERA5 and in South America for HRES. While HRES DSTDs in all regions having a negative slope, except in Japan where a limited correlation (0.01) is observed, ERA5 DSTDs exert clear positive slope with the elevation in Eastern Europe, Japan, and New Zealand, indicating its relatively poorer agreements with GPS than HRES at high altitudes.

It is shown in Figure 6 that, apart from western North America, a majority of GPS stations are installed at low altitudes (<1 km). Therefore, to investigate further the elevation dependency of the weather model
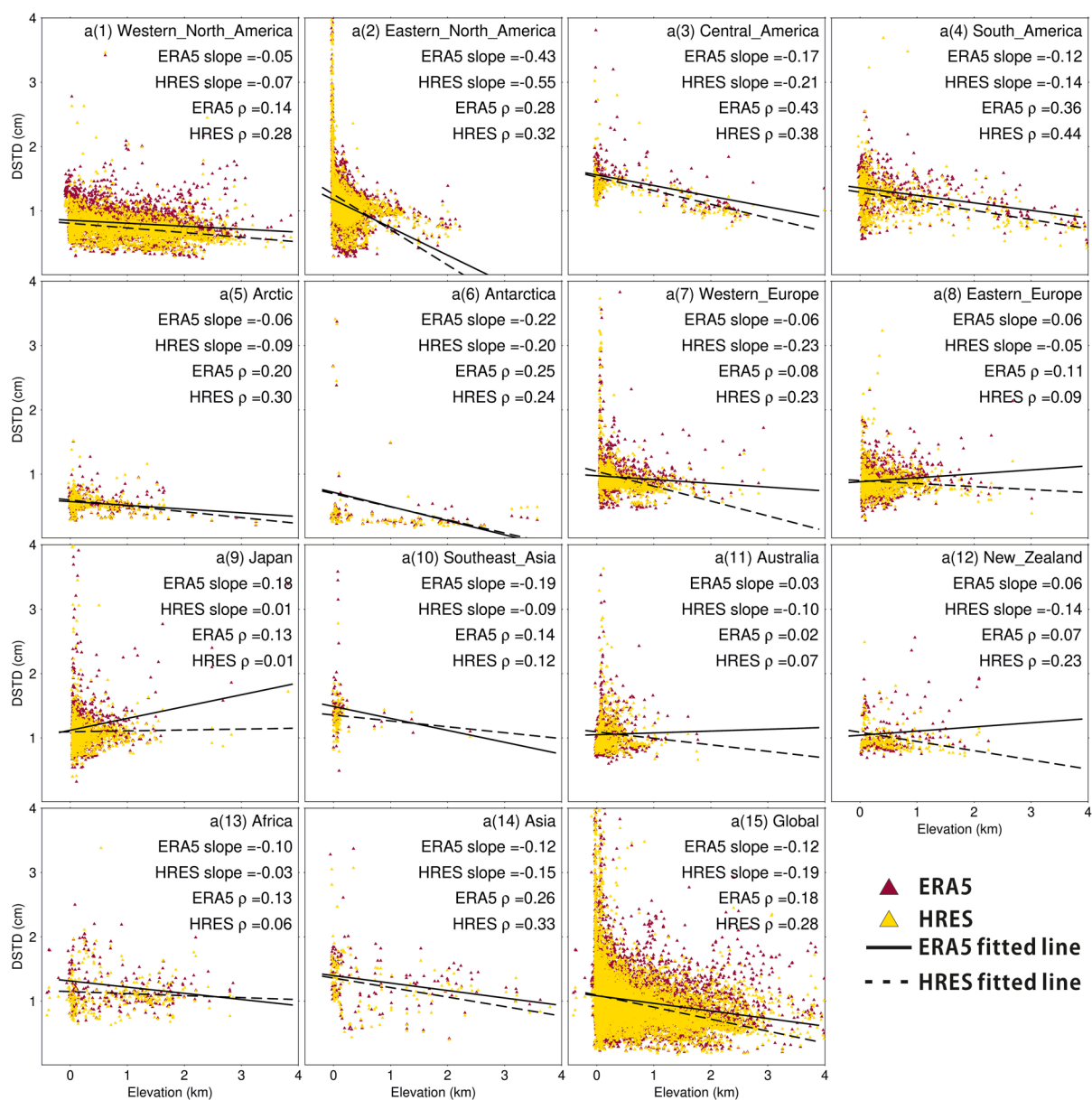
Figure 6. Elevation dependency of DSTDs respectively between ERA5 and GPS ZTDs (red) and between HRES and GPS ZTDs (yellow) using 3 years of data from January 2016 to December 2018. The slope is defined in a linear relationship (DSTD = slope × elevation + intercept). Regions are defined in Figure 1a1. DSTD, Difference STandard Deviation; GPS, Global Positioning System; HRES, High RESolution; ZTD, Zenith Tropospheric Delay.

performances especially at high altitudes, we plotted in Figure 7 the PWV DSTD against the elevation per MODIS pixel, which provides more high-altitude samples than GPS. A clear PWV DSTD elevation dependency is observed in nearly all regions, with an average slope of −0.06 for ERA5 and −0.05 for HRES, corresponding to a decrease of DSTD of 0.06 and 0.05 cm per 1 km, respectively. The largest slope (absolute values, the same hereinafter) occurs in Africa where the DSTD drops the fastest as the elevation increases, whereas eastern North America has the gentlest slope partly due to its flat topography. There are large disturbances at high altitude pixels in Antarctica (Figure 7a6), and also in some parts of Arctic (Figure 7a5), due to the problematic quality of the MODIS PWV over these areas. The global averaged correlation coefficients, excluding Antarctica, are 0.33 between ERA5 and MODIS, and 0.31 between HRES and MODIS.
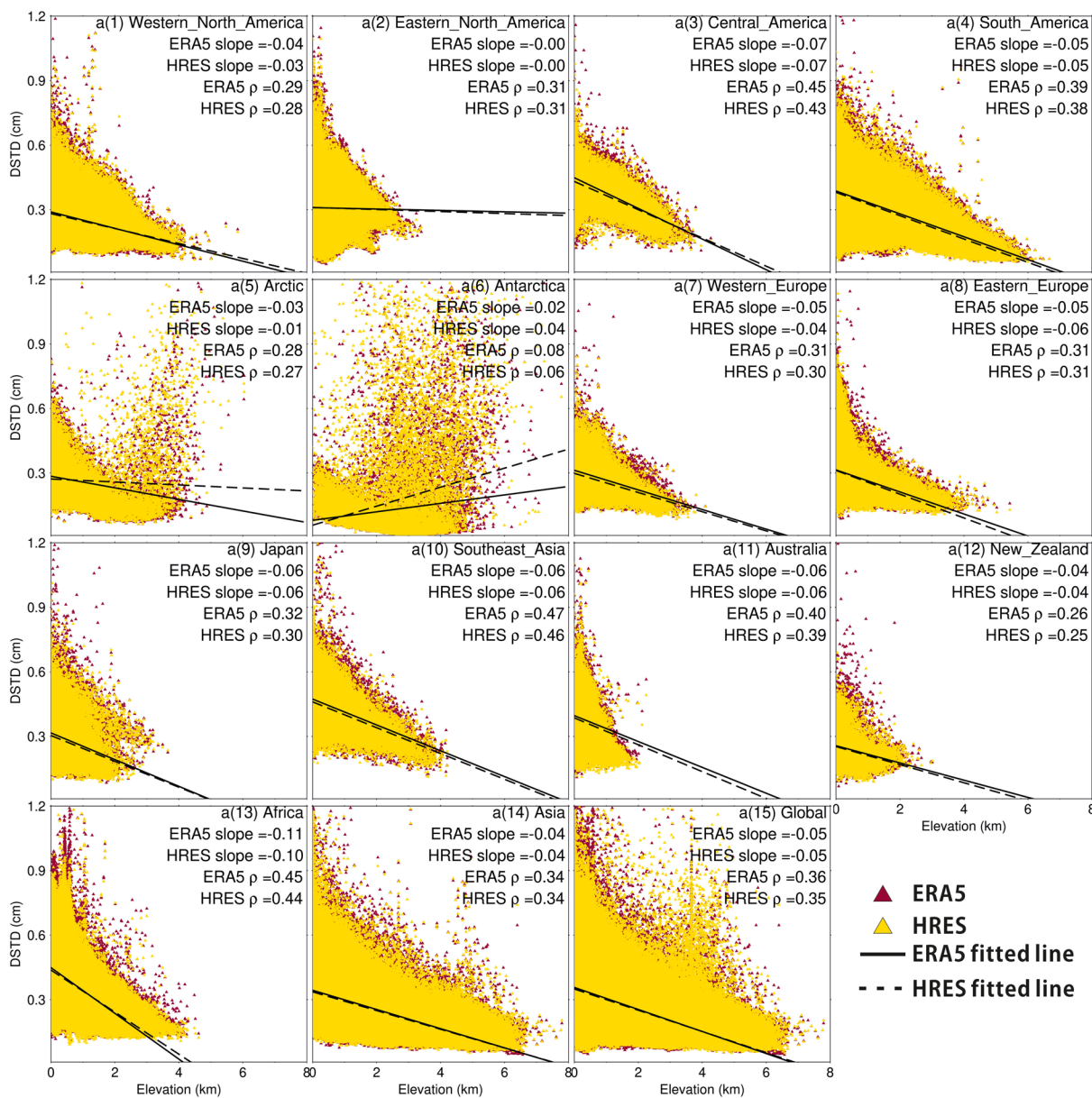
Figure 7. Elevation dependency of DSTDs respectively between ERA5 and MODIS PWV (red) and between HRES and MODIS PWV (yellow) using 3 years of cloud free MODIS data. The slope is defined in a linear relationship (DSTD = slope × elevation + intercept). Regions are defined in Figure 1a1. DSTD, Difference STandard Deviation; HRES, High RESolution; MODIS, Moderate Resolution Imaging Spectrometer; PWV, precipitable water vapor.

5.2. Magnitude Dependency

As Sections 5.1 shows that ZTD/PWV DSTDs generally decrease with the elevation, it is necessary to investigate its dependence on the magnitudes of the ZTD and PWV, given the fact that their magnitudes also generally decrease with the elevation. These are showed in Figure 8 using 3 years of data, with the magnitude dependency represented as the relative DSTD, defined as the percentage relative to the 3-year mean magnitude of the ZTD at a GPS station or PWV at a MODIS pixel. Figure 8a shows that the average relative DSTD are 0.44% for ERA5 and 0.43% for HRES, respectively. Forty-three and eight tenths percentage of GPS stations have a relative ERA5 DSTD that is below 0.6% compared to 47.8% for HRES DSTDs. Large relative DSTD differences between ERA5 and HRES ZTDs occur mostly in the western coast of North America, with a global mean difference of 0.02%. Figure 8b shows that the global average relative PWV DSTD, excluding Antarctica, are 18.25% for ERA5 and 17.88% for HRES, respectively. 63% of pixels have a relative ERA5 PWV
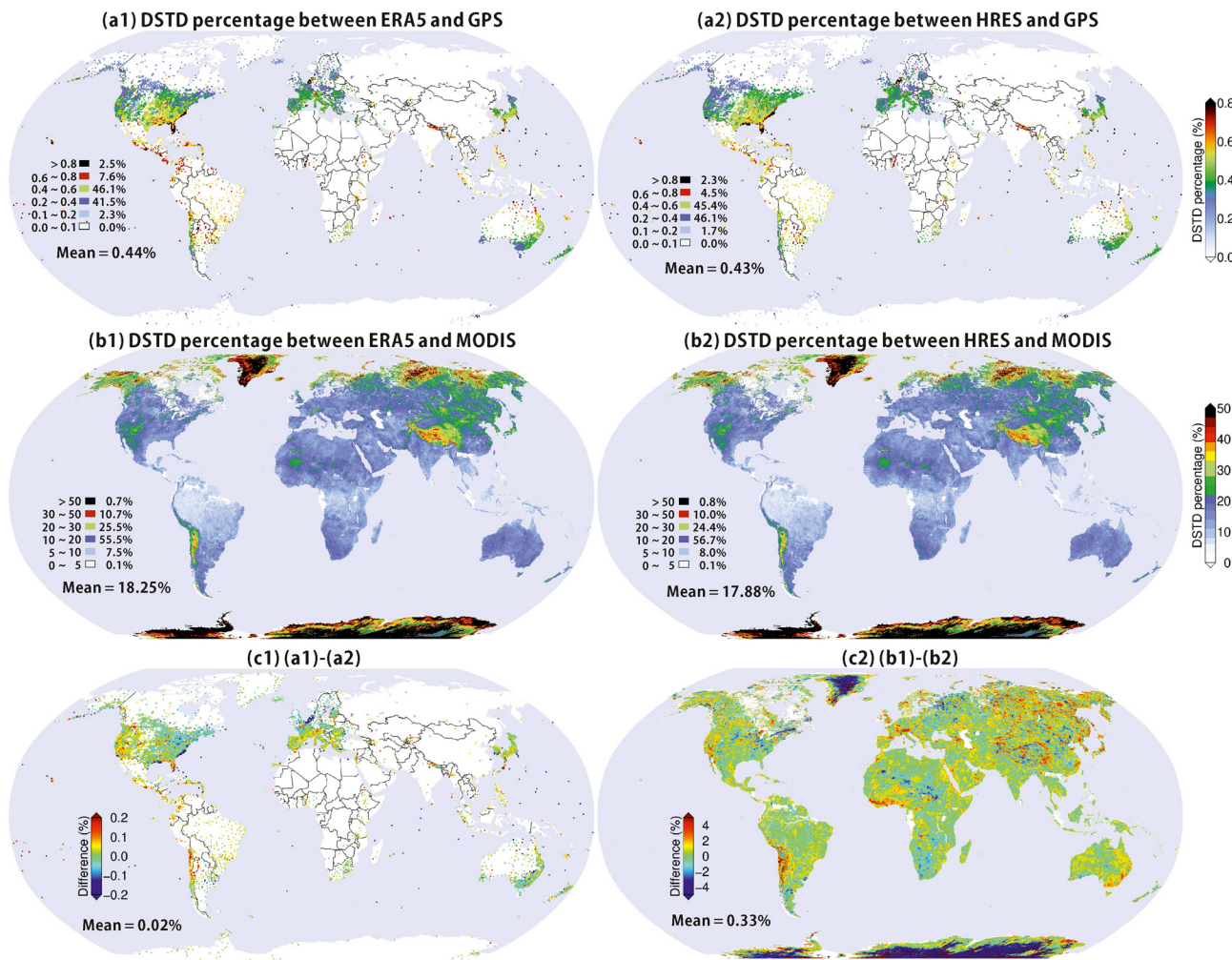
Figure 8. Magnitude dependency of DSTDs respectively between ERA5 and GPS ZTDs (a1), between ERA5 and MODIS PWV (b1), between HRES and GPS ZTDs (a2) and between HRES and MODIS PWV (b2). (c1) shows the difference between (a1 and a2). (c2) shows the difference between (b1 and b2). DSTD, Difference STandard Deviation; GPS, Global Positioning System; HRES, High RESolution; MODIS, Moderate Resolution Imaging Spectrometer; PWV, Precipitable water vapor; ZTD, Zenith Tropospheric Delay.

DSTD that is below 20% compared to 64.7% for HRES. Large relative PWV DSTD differences between ERA5 and HRES occur mostly in the south of the Andes, the coast of the Gulf of Guinea and the southeast coast of Australia where the relative DSTD differences exceed 3%. Special care should be taken in areas with low amounts of water vapor hence low PWV DSTDs. For example, although regions such as the Tibet plateau, Andes and Alaska have low PWV DSTDs as shown in Figure 4, their relative PWV DSTD are higher (>35%) compared to their surrounding areas, indicating poor agreements with MODIS in terms of the relative accuracy. This could be caused by their rough and variated topography. Tables 1 and 2 give the detailed relative DSTD for each region.

5.3. Importance of Temporal Resolution

Figure 3 has shown that the DSTD between HRES and GPS ZTDs in some regions varies at each hour of the day, given the fact that the hourly HRES ZTDs were linearly interpolated from the 6 h sampled HRES ZTDs. However, these statistics were obtained from averaging all stations so that the effect of the temporal interpolation may not be substantially visible. To highlight this effect and the benefit of the high temporal resolution of ERA5, we present in Figure 9 the hourly ZTD differences respectively between HRES and GPS (red lines), and between ERA5 and GPS (blue lines) during storm Aileen in the United Kingdom from 11 to

Table 1
ZTD Comparison Statistics With Respect to GPS for Each Region Defined in Figure 1a1 and for the Globe

Region name	Number of stations	Mean difference (cm)		Mean DSTD (cm)		Mean DSTD percentage (%)		Slope (cm per km)	
		ERA5	HRES	ERA5	HRES	ERA5	HRES	ERA5	HRES
Western North America	3,172	−0.01	−0.15	1.25	0.88	0.39	0.35	−0.05	−0.07
Eastern North America	3,629	−0.59	−0.65	1.15	1.21	0.45	0.47	−0.43	−0.55
Central America	267	0.43	0.40	1.97	1.64	0.62	0.59	−0.17	−0.21
South America	685	1.21	1.18	1.64	1.37	0.55	0.51	−0.12	−0.14
Arctic	344	0.8	0.56	1.15	0.95	0.24	0.25	−0.06	−0.09
Antarctica	114	−1.1	−0.78	1.97	1.04	0.26	0.25	−0.22	−0.20
Western Europe	1,300	1.67	1.66	1.19	1.03	0.41	0.41	−0.06	−0.23
Eastern Europe	1,188	1.25	1.35	1.29	0.98	0.39	0.38	−0.06	−0.05
Japan	1,603	1.6	1.59	1.37	1.13	0.49	0.46	0.18	0.01
Southeast Asia	109	1.26	1.14	2.14	1.78	0.57	0.55	−0.19	−0.09
Australia	725	1.16	1.09	1.54	1.53	0.44	0.45	−0.03	−0.10
New Zealand	237	0.81	1.33	1.58	1.19	0.47	0.44	−0.06	−0.14
Africa	274	0.77	1.20	2.06	1.26	0.55	0.5	−0.10	−0.03
Asia	161	−0.04	−0.48	1.85	1.50	0.57	0.54	−0.12	−0.15
Global	13,808	0.46	0.43	1.69	1.54	0.44	0.43	−0.12	−0.19

Abbreviations: GPS, Global Positioning System; ZTD, Zenith Tropospheric Delay.

Table 2
PWV Comparison Statistics With Respect to MODIS for Each Region Defined in Figure 1a1 and for the Globe

Region name	Number of pixels (million)	Mean difference (cm)		Mean DSTD (cm)		Mean DSTD percentage (%)		Slope (cm per km)	
		ERA5	HRES	ERA5	HRES	ERA5	HRES	ERA5	HRES
Western North America	209.8	−0.15	−0.15	0.21	0.20	24.07	23.71	−0.04	−0.03
Eastern North America	161.0	−0.25	−0.24	0.21	0.21	18.67	18.64	0.00	0.00
Central America	21.9	−0.55	−0.54	0.39	0.36	12.66	12.30	−0.07	−0.07
South America	296.0	−0.58	−0.55	0.35	0.34	12.71	12.42	−0.05	−0.05
Arctic	287.6	−0.07	−0.06	0.19	0.20	30.66	30.37	−0.03	−0.01
Antarctica[a]	80.3	0.29	0.30	0.45	0.50	49.07	50.19	−0.02	−0.04
Western Europe	51.6	−0.24	−0.22	0.24	0.22	19.17	18.28	−0.05	−0.04
Eastern Europe	234.5	−0.20	−0.19	0.23	0.22	19.26	19.01	−0.05	−0.06
Japan	48.0	−0.19	−0.18	0.24	0.22	21.73	20.93	−0.06	−0.06
Southeast Asia	21.5	−0.63	−0.61	0.46	0.43	9.08	8.80	−0.06	−0.06
Australia	265.9	−0.56	−0.54	0.32	0.31	16.07	15.57	−0.06	−0.06
New Zealand	5.0	−0.14	−0.12	0.29	0.27	17.96	17.70	−0.04	−0.04
Africa	1,081.4	−0.49	−0.51	0.35	0.34	14.79	14.62	−0.11	−0.10
Asia	596.0	−0.26	−0.26	0.26	0.25	20.46	20.03	−0.04	−0.04
Global[b]	3,280.2	−0.33	−0.32	0.34	0.32	18.25	17.88	−0.05	−0.05

[a]Due to the ice cover deteriorating the quality of the MODIS PWV, the statistics of Antarctica may not reflect the true quality of the weather model. [b]The global statistics were calculated excluding pixels over Antarctica.
Abbreviations: DSTD, Difference STandard Deviation; MODIS, Moderate Resolution Imaging Spectrometer; PWV, precipitable water vapor.
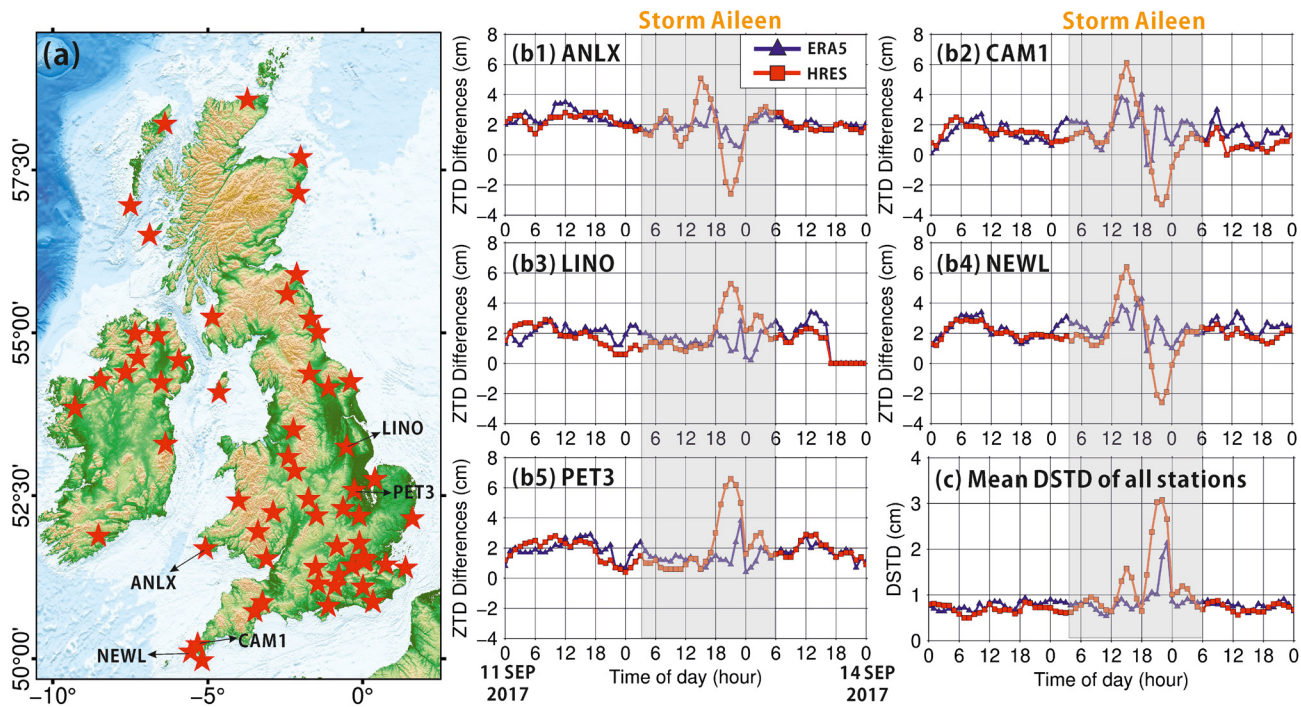
Figure 9. ZTD differences between ERA5 and GPS (blue), and between HRES and GPS (red) during storm Aileen from 11 to 14 September 2017. (c) is the 3 day mean DSTD of all the stations displayed in (a). DSTD, Difference STandard Deviation; GPS, Global Positioning System; HRES, High RESolution; ZTD, Zenith Tropospheric Delay.

14 September 2017. Since the GPS ZTD is sampled every 5 min, it is sufficient to capture the ZTD variation during the whole process of the storm and is served as the ground truth to validate the two weather models. Figure 9b shows that before and after the storm, the two weather models performed similarly. However, HRES failed at predicting the ZTD during the storm and performed much poorer than ERA5. The high temporal resolution of ERA5 indeed improved its capability of capturing the rapid changing ZTD during the storm, with a more stable ZTD difference with GPS than HRES. The HRES ZTD differed from GPS the most at 15:00 and 21:00 of 12 September when there is a 3-h time difference against the original HRES ZTD samples. It is also noticed that there is a constant ~2 cm offset between the two weather models and GPS ZTDs which is also observed in Figure 1a. The mean DSTD of all stations in Figure 9a for ERA5 during the stormy hours from 3:00 12 September to 6:00 13 September is 0.89 cm, compared to 1.20 cm for HRES, improving 26% despite ERA5 having a lower spatial resolution than HRES. As a result, one cannot rely on the temporal linear interpolation under such extreme weather conditions and it is important to take account the time difference into consideration when utilizing these two weather models.

With the proliferation of recent (Sentinel-1) and planned (e.g., GEOSAR and NISAR) InSAR missions having wider coverage of potentially up to 1,000 km, the spatial-temporally correlated water vapor effect, which increases with distance and may indistinguishable from other long wavelength effects such as the ocean tide loading (e.g., Yu et al., 2020) and the solid tide loading (e.g., Xu & Sandwell, 2019), becomes increasingly dominant and is now crucial in nationwide or continent-wide deformation mapping and in studies of Glacial Isostatic Adjustment (GIA), inter-seismic tectonic strain accumulation, post-seismic relaxation, slow slip events and creeping of fault systems where the weather models play an important role. The comparisons in this study may provide guidelines of applying the weather models to such applications and provide comprehensive implications to users when deciding which weather model to use at different acquisition times and locations.

6. Conclusions

We have validated the ERA5 and HRES weather models by the GPS ZTD and MODIS PWV, respectively, using 3 years of data from January 2016 to December 2018 of every 1 h. The global mean ZTD differences with respect to GPS are 0.49 cm for ERA5 and 0.43 cm for HRES, and the global ZTD DSTDs are 1.69 cm for ERA5 and 1.54 cm for HRES. The global mean PWV differences with respect to MODIS are −0.32 cm for ERA5 and −0.31 cm for HRES, and the global PWV DSTDs are 0.34 cm for ERA5 and 0.32 cm for HRES.

The two weather models generally perform better in regions of western and eastern North America, Europe, and Arctic where the mean DSTDs are less than 1.3 cm as revealed by GPS. HRES also has a low DSTD of less than 1.3 cm in Antarctic, Japan, New Zealand, and Africa. Although regions such as the Tibet plateau, Andes, and Alaska have low PWV DSTDs (<0.2 cm) as shown in Figure 4, the relative PWV DSTD shown in Figure 8 are much higher (>35%) than the global average (∼18%). Clear DSTD seasonal variations are observed in mid-latitude areas due to seasonal changes in the water vapor compared to Equatorial (all year high) and Polar (all year low) regions. Detailed statistics for each region are shown in Tables 1 and 2.

HRES generally performs better than ERA5 revealed by GPS and MODIS, despite the fact that 83% of its ZTD and PWV values were temporally interpolated. HRES also has a lower PWV DSTD in the coast of Gulf of Guinea, eastern edge of Andes, southeast of China, and southeast of Australia (Figure 4c2). However, under extreme weather conditions with sudden changes of ZTDs, as in Section 5.3, ERA5 performs better than HRES at epochs that are far from the HRES sampling hours (i.e., 3, 9, 15, 21 o'clock in UTC). One should take account both the spatial and temporal resolution into consideration when utilizing the two weather models.

The performance of the two weather models with respect to GPS and MODIS are dependent on both the elevation and the magnitude of the ZTD or PWV. Comparisons with GPS ZTDs reveal global mean slopes (between the DSTD and elevation) of −0.12 for ERA5 and −0.19 for HRES, corresponding to a decrease of ZTD DSTD of 0.12 and 0.19 cm per 1 km, respectively. Comparisons with MODIS PWV reveal global mean slopes (between the PWV DSTD and elevation) of −0.06 for ERA5 and −0.04 for HRES, corresponding to a decrease of DSTD of 0.06 and 0.04 cm per 1 km, respectively. Depending on the magnitudes, the global mean ZTD DSTDs account for 0.44% and 0.43% of the mean ZTD for ERA5 and HRES, respectively, and the global mean PWV DSTDs account for 18.25% and 17.88% of the mean PWV for ERA5 and HRES, respectively.

Data Availability Statement

The MODIS data and the SRTM DEM used in this paper were obtained from the Land Processes Distributed Active Archive Centre (LP DAAC). The ASTER GDEM was obtained from NASA Earthdata (https://search.earthdata.nasa.gov/search). The HRES data was obtained from ECMWF (https://apps.ecmwf.int/archive-catalogue/?type=an%26class=od%26stream=oper%26expver=1) and the ERA5 data was obtained from (https://cds.climate.copernicus.eu/#!/search?text=ERA5&type=dataset). The GPS data was obtained from the Nevada Geodetic Laboratory (http://geodesy.unr.edu/gps_timeseries).

References

Ahmed, F., Václavovic, P., Teferle, F. N., Douša, J., Bingley, R., & Laurichesse, D. (2016). Comparative analysis of real-time precise point positioning zenith total delay estimates. *GPS Solutions*, *20*, 187–199. https://doi.org/10.1007/s10291-014-0427-z

Anantrasirichai, N., Biggs, J., Albino, F., & Bull, D. (2019). A deep learning approach to detecting volcano deformation from satellite imagery using synthetic datasets. *Remote Sensing of Environment*, *230*, 111179. https://doi.org/10.1016/j.rse.2019.04.032

Barbarella, M., Di Benedetto, A., Fiani, M., Guida, D., & Lugli, A. (2018). Use of DEMs derived from TLS and HRSI data for landslide feature recognition. *International Journal of Geo-Information*, *7*, 160. https://doi.org/10.3390/ijgi7040160

Bevis, M., Businger, S., Chiswell, S., Herring, T. A., Anthes, R. A., Rocken, C., & Ware, R. H. (1994). GPS meteorology: Mapping zenith wet delays onto precipitable water. *Journal of Applied Meteorology*, *33*, 379–386. https://doi.org/10.1175/1520-0450(1994)033<0379:gmmzwd>2.0.co;2

Bevis, M., Businger, S., Herring, T. A., Rocken, C., Anthes, R. A., & Ware, R. H. (1992). GPS meteorology: Remote sensing of atmospheric water vapor using the global positioning system. *Journal of Geophysical Research*, *97*, 15787. https://doi.org/10.1029/92jd01517

Blewitt, G., Kreemer, C., Hammond, W. C., & Gazeaux, J. (2016). MIDAS robust trend estimator for accurate GPS station velocities without step detection. *Journal of Geophysical Research: Solid Earth*, *121*, 2054–2068. https://doi.org/10.1002/2015jb012552

Boehm, J., & Schuh, H. (2007). Troposphere gradients from the ECMWF in VLBI analysis. *Journal of Geodesy*, *81*, 403–408. https://doi.org/10.1007/s00190-007-0144-2

Bordi, I., Zhu, X., & Fraedrich, K. (2016). Precipitable water vapor and its relationship with the Standardized Precipitation Index: ground-based GPS measurements and reanalysis data. *Theoretical and Applied Climatology*, *123*, 263–275. https://doi.org/10.1007/s00704-014-1355-0

Chelton, D. B., Hussey, K. J., & Parke, M. E. (1981). Global satellite measurements of water vapor, wind speed and wave height. *Nature*, *294*, 529–532. https://doi.org/10.1038/294529a0

Chen, Q., Song, S., Heise, S., Liou, Y.-A., Zhu, W., & Zhao, J. (2011). Assessment of ZTD derived from ECMWF/NCEP data with GPS ZTD over China. *GPS Solutions*, *15*, 415–425. https://doi.org/10.1007/s10291-010-0200-x

Cliffe Ssenyunzi, R., Oruru, B., Mutonyi D'ujanga, F., Realini, E., Barindelli, S., Tagliaferro, G., et al. (2020). Performance of ERA5 data in retrieving precipitable water vapor over East African tropical region. *Advances in Space Research*. https://doi.org/10.1016/j.asr.2020.02.003

Daout, S., Sudhaus, H., Kausch, T., Steinberg, A., & Dini, B. (2019). Interseismic and postseismic shallow creep of the North Qaidam thrust faults detected with a multitemporal InSAR analysis. *Journal of Geophysical Research: Solid Earth*, *124*, 7259–7279. https://doi.org/10.1029/2019jb017692

Davis, J. L., Herring, T. A., Shapiro, I. I., Rogers, A. E. E., & Elgered, G. (1985). Geodesy by radio interferometry: Effects of atmospheric modeling errors on estimates of baseline length. *Radio Science*, *20*, 1593–1607. https://doi.org/10.1029/rs020i006p01593

Durre, I., Yin, X., Vose, R. S., Applequist, S., & Arnfield, J. (2018). Enhancing the data coverage in the integrated Global Radiosonde Archive. *Journal of Atmospheric and Oceanic Technology*, *35*, 1753–1770. https://doi.org/10.1175/jtech-d-17-0223.1

Elgered, G., Davis, J. L., Herring, T. A., & Shapiro, I. I. (1991). Geodesy by radio interferometry: Water vapor radiometry for estimation of the wet delay. *Journal of Geophysical Research*, *96*, 6541–6555. https://doi.org/10.1029/90jb00834

Eriksson, D., Macmillan, D. S., & Gipson, J. M. (2014). Tropospheric delay ray tracing applied in VLBI analysis. *Journal of Geophysical Research: Solid Earth*, *119*, 9156–9170. https://doi.org/10.1002/2014jb011552

Esposito, G., Salvini, R., Matano, F., Sacchi, M., & Troise, C. (2018). Evaluation of geomorphic changes and retreat rates of a coastal pyroclastic cliff in the Campi Flegrei volcanic district, southern Italy. *Journal of Coastal Conservation*, *22*, 957–972. https://doi.org/10.1007/s11852-018-0621-1

Farr, T. G., Rosen, P. A., Caro, E., Crippen, R., Duren, R., Hensley, S., et al. (2007). The shuttle radar topography mission. *Reviews of Geophysics*, *45*, RG2004. https://doi.org/10.1029/2005rg000183

Frey, R. A., Ackerman, S. A., Liu, Y., Strabala, K. I., Zhang, H., Key, J. R., & Wang, X. (2008). Cloud detection with MODIS. Part I: Improvements in the MODIS cloud mask for Collection 5. *Journal of Atmospheric and Oceanic Technology*, *25*, 1057–1072. https://doi.org/10.1175/2008jtecha1052.1

Gaffen, D. J., & Ross, R. J. (1999). Climatology and trends of U.S. surface humidity and temperature. *Journal of Climate*, *12*, 811–828. https://doi.org/10.1175/1520-0442(1999)012<0811:catous>2.0.co;2

Gao, B.-C., & Kaufman, Y. J. (2003). Water vapor retrievals using Moderate Resolution Imaging Spectroradiometer (MODIS) near-infrared channels. *Journal of Geophysical Research*, *108*, 4389. https://doi.org/10.1029/2002jd003023

Georgiev, C. G. (2003). Use of data from Meteosat water vapor channel and surface observations for studying pre-convective environment of a tornado-producing storm. *Atmospheric Research*, *67–68*, 231–246. https://doi.org/10.1016/s0169-8095(03)00054-1

Gurbuz, G., & Jin, S. (2017). Long-time variations of precipitable water vapor estimated from GPS, MODIS and radiosonde observations in Turkey. *International Journal of Climatology*, *37*, 5170–5180. https://doi.org/10.1002/joc.5153

Gutman, S. I., & Benjamin, S. G. (2001). The role of ground-based GPS meteorological observations in numerical weather prediction. *GPS Solutions*, *4*, 16–24. https://doi.org/10.1007/pl00012860

Hu, G. R., Khoo, H. S., Goh, P. C., & Law, C. L. (2003). Development and assessment of GPS virtual reference stations for RTK positioning. *Journal of Geodesy*, *77*, 292–302. https://doi.org/10.1007/s00190-003-0327-4

Hu, Z., & Mallorquí, J. J. (2019). An accurate method to correct atmospheric phase delay for InSAR with the ERA5 global atmospheric model. *Remote Sensing*, *11*, 1969. https://doi.org/10.3390/rs11171969

Iwabuchi, T., Miyazaki, S., Heki, K., Naito, I., & Hatanaka, Y. (2003). An impact of estimating tropospheric delay gradients on tropospheric delay estimations in the summer using the Japanese nationwide GPS array. *Journal of Geophysical Research*, *108*. https://doi.org/10.1029/2002jd002214

Jiang, C., Xu, T., Wang, S., Nie, W., & Sun, Z. (2020). Evaluation of zenith tropospheric delay derived from ERA5 data over China using GNSS observations. *Remote Sensing*, *12*, 663. https://doi.org/10.3390/rs12040663

Jolivet, R., Agram, P. S., Lin, N. Y., Simons, M., Doin, M. P., Peltzer, G., & Li, Z. (2014). Improving InSAR geodesy using Global Atmospheric Models. *Journal of Geophysical Research: Solid Earth*, *119*, 2324–2341. https://doi.org/10.1002/2013jb010588

Jolivet, R., Grandin, R., Lasserre, C., Doin, M. P., & Peltzer, G. (2011). Systematic InSAR tropospheric phase delay corrections from global meteorological reanalysis data. *Geophysical Research Letters*, *38*. https://doi.org/10.1029/2011gl048757

Jolivet, R., Lasserre, C., Doin, M.-P., Peltzer, G., Avouac, J.-P., Sun, J., & Dailu, R. (2013). Spatio-temporal evolution of aseismic slip along the Haiyuan fault, China: Implications for fault frictional properties. *Earth and Planetary Science Letters*, *377–378*, 23–33. https://doi.org/10.1016/j.epsl.2013.07.020

Joly, M., & Voldoire, A. (2010). Role of the Gulf of Guinea in the inter-annual variability of the West African monsoon: What do we learn from CMIP3 coupled simulations? *International Journal of Climatology*, *30*, 1843–1856. https://doi.org/10.1002/joc.2026

Kiehl, J. T., & Trenberth, K. E. (1997). Earth's Annual Global Mean Energy Budget. *Bulletin of the American Meteorological Society*, *78*, 197–208. https://doi.org/10.1175/1520-0477(1997)078<0197:eagmeb>2.0.co;2

Li, Z., Fielding, E. J., & Cross, P. (2009). Integration of InSAR time-series analysis and water-vapor correction for emapping postseismic motion after the 2003 Bam (Iran) earthquake. *IEEE Transactions on Geoscience and Remote Sensing*, *47*, 3220–3230. https://doi.org/10.1109/TGRS.2009.2019125

Li, Z., Muller, J. P., & Cross, P. (2003). Comparison of precipitable water vapor derived from radiosonde, GPS, and Moderate-Resolution Imaging Spectroradiometer measurements. *Journal of Geophysical Research*, *108*, 4651. https://doi.org/10.1029/2003jd003372

Li, Z., Muller, J. P., Cross, P., & Fielding, E. J. (2005). Interferometric synthetic aperture radar (InSAR) atmospheric correction: GPS, Moderate Resolution Imaging Spectroradiometer (MODIS), and InSAR integration. *Journal of Geophysical Research*, *110*, 1–10. https://doi.org/10.1029/2004jb003446

Lin, H., You, Q., Zhang, Y., Jiao, Y., & Fraedrich, K. (2016). Impact of large-scale circulation on the water vapor balance of the Tibetan Plateau in summer. *International Journal of Climatology*, *36*, 4213–4221. https://doi.org/10.1002/joc.4626

Liu, Z., Wong, M. S., Nichol, J., & Chan, P. W. (2013). A multi-sensor study of water vapor from radiosonde, MODIS and AERONET: A case study of Hong Kong. *International Journal of Climatology*, *33*, 109–120. https://doi.org/10.1002/joc.3412

Meng, X., Roberts, S., Cui, Y., Gao, Y., Chen, Q., Xu, C., et al. (2018). Required navigation performance for connected and autonomous vehicles: Where are we now and where are we going? *Transportation Planning and Technology*, *41*, 104–118. https://doi.org/10.1080/03081060.2018.1402747

Millán, M. M. (2014). Extreme hydrometeorological events and climate change predictions in Europe. *Journal of Hydrology*, *518*, 206–224. https://doi.org/10.1016/j.jhydrol.2013.12.041

Mori, N., Takahashi, T., Yasuda, T., & Yanagisawa, H. (2011). Survey of 2011 Tohoku earthquake tsunami inundation and run-up. *Geophysical Research Letters*. https://doi.org/10.1029/2011GL049210

Murray, K. D., Bekaert, D. P. S., & Lohman, R. B. (2019). Tropospheric corrections for InSAR: Statistical assessments and applications to the Central United States and Mexico. *Remote Sensing of Environment*, *232*. https://doi.org/10.1016/j.rse.2019.111326

Obligis, E., Desportes, C., Eymard, L., Fernandes, M. J., Lázaro, C., & Nunes, A. L. (2011). Tropospheric corrections for coastal altimetry. In *Coastal altimetry* (pp. 147–176). Springer Berlin Heidelberg. https://doi.org/10.1007/978-3-642-12796-0_6

Prasad, A. K., & Singh, R. P. (2009). Validation of MODIS Terra, AIRS, NCEP/DOE AMIP-II Reanalysis-2, and AERONET Sun photometer derived integrated precipitable water vapor using ground-based GPS receivers over India. *Journal of Geophysical Research*, *114*, D05107. https://doi.org/10.1029/2008jd011230

Price, C. (2000). Evidence for a link between global lightning activity and upper tropospheric water vapor. *Nature*, *406*, 290–293. https://doi.org/10.1038/35018543

Stallo, C., Neri, A., Salvatori, P., Capua, R., & Rispoli, F. (2018). GNSS Integrity Monitoring for Rail Applications: 2-tiers method. *IEEE Transactions on Aerospace and Electronic Systems*, *55*, 1850–1863. https://doi.org/10.1109/TAES.2018.2876735

Team, A. G. V. (2011). *ASTER global digital elevation model version 2—Summary of validation results, Japan Space Systems*. NASA. https://doi.org/10.1017/CBO9781107415324.004

Vaquero-Martínez, J., Antón, M., Ortiz de Galisteo, J. P., Cachorro, V. E., Costa, M. J., Román, R., & Bennouna, Y. S. (2017). Validation of MODIS integrated water vapor product against reference GPS data at the Iberian Peninsula. *International Journal of Applied Earth Observation and Geoinformation*, *63*, 214–221. https://doi.org/10.1016/j.jag.2017.07.008

Veljović, K., & Vujović, D. (2019). Climatology of fog occurrence over a wide flat area in Serbia based on visibility observations. *International Journal of Climatology*, *39*, 1331–1344. https://doi.org/10.1002/joc.5883

Vonder Haar, T. H., Bytheway, J. L., & Forsythe, J. M. (2012). Weather and climate analyses using improved global water vapor observations. *Geophysical Research Letters*, *39*. https://doi.org/10.1029/2012gl052094

Webb, T. L., Wadge, G., & Pascal, K. (2020). Mapping water vapor variability over a mountainous tropical island using InSAR and an atmospheric model for geodetic observations. *Remote Sensing of Environment*, *237*. https://doi.org/10.1016/j.rse.2019.111560

Webley, P. W., Bingley, R. M., Dodson, A. H., Wadge, G., Waugh, S. J., & James, I. N. (2002). Atmospheric water vapor correction to InSAR surface motion measurements on mountains: Results from a dense GPS network on Mount Etna. *Physics and Chemistry of the Earth, Parts A/B/C*, *27*, 363–370. https://doi.org/10.1016/s1474-7065(02)00013-x

Xu, X., & Sandwell, D. T. (2019). Toward absolute phase change recovery with InSAR: Correcting for earth tides and phase unwrapping ambiguities. *IEEE Transactions on Geoscience and Remote Sensing*, *58*, 726–733. https://doi.org/10.1109/tgrs.2019.2940207

Yip, S. T. H., Biggs, J., & Albino, F. (2019). Reevaluating volcanic deformation using atmospheric corrections: Implications for the magmatic system of Agung Volcano, Indonesia. *Geophysical Research Letters*, *46*, 13704–13711. https://doi.org/10.1029/2019gl085233

Yu, C., Li, Z., Penna, N. T., & Crippa, P. (2018). Generic atmospheric correction model for interferometric synthetic aperture radar observations. *Journal of Geophysical Research: Solid Earth*, *123*, 9202–9222. https://doi.org/10.1029/2017jb015305

Yu, C., Penna, N. T., & Li, Z. (2017). Generation of real-time mode high-resolution water vapor fields from GPS observations. *Journal of Geophysical Research: Atmospheres*, *122*, 2008–2025. https://doi.org/10.1002/2016jd025753

Yu, C., Penna, N., & Li, Z. (2020). Ocean tide loading effects on InSAR observations over wide regions. *Geophysical Research Letters*, *47*, e2020GL088184. https://doi.org/10.1029/2020gl088184

Zahorec, P., Papčo, J., Vajda, P., Greco, F., Cantarero, M., & Carbone, D. (2018). Refined prediction of vertical gradient of gravity at Etna volcano gravity network (Italy). *Contributions to Geophysics and Geodesy*, *48*, 299–317. https://doi.org/10.2478/congeo-2018-0014

Zhu, K., Zhao, L., Wang, W., Zhang, S., Liu, R., & Wang, J. (2018). Augment BeiDou real-time precise point positioning using ECMWF data. *Earth, Planets and Space*, *70*, 112. https://doi.org/10.1186/s40623-018-0870-0